Proceedings of the ASME 2010 3rd Joint US-European Fluids Engineering Summer Meeting and 8th International Conference on Nanochannels, Microchannels, and Minichannels
FEDSM-ICNMM2010
August 1-5, 2010, Montreal, Canada

FEDSM-ICNMM2010-30092

IMPULSIVE PLUNGING WAVE BREAKING DOWNSTREAM OF A BUMP IN A SHALLOW WATER FLUME

Bonguk Koo, Zhaoyuan Wang, Jianming Yang, Donghoon Kang[1], and Frederick Stern
IIHR-Hydroscience & Engineering, University of Iowa, Iowa City, IA, 52242, USA

ABSTRACT

The plunging wave-breaking process for impulsive flow over a bump in a shallow water flume is described using complementary experiments and simulations, which is relevant to ship hydrodynamics since it includes effects of wave-body interactions and wave breaking direction is opposite to the mean flow. Phase averaged measurements (relative to the time at which the maximum wave height is reached just before the first plunge) are conducted, including the overall flume flow and 2D PIV center-plane velocities and turbulence inside the plunging breaking wave and bottom pressures under the breaking wave. A total number of 226 individual plunging wave-breaking tests were conducted, which all followed a similar time line consisting of startup, steep wave formation, plunging wave, and chaotic wave breaking swept downstream time phases. The plunging wave breaking process consists of four repeated plunging events each with three [jet impact (plunge), oblique splash and vertical jet] sub-events, which were identified first using complementary CFD. Video images with red dye display the plunging wave breaking events and sub-events. The first and second plunges take longer than the last two plunges. Oblique splashes and vertical jets account for more time than plunging. The wave profile at maximum height, first plunge, bump and wave breaking vortex and entrapped air bubble trajectories, entrapped air bubble diameters, kinetic, potential, and total energy, and bottom pressures are analyzed. The simulations on four different grids qualitatively predict all four time phases, all four plunging events and their sub-events, and bottom pressure but with reduced velocity magnitudes and larger post-breaking water elevations. The medium grid results are presented and the fine grid simulations are in progress. Similarities and differences are discussed with the previous deep water or sloping beaches experimental and computational studies.

INTRODUCTION

Most studies on plunging wave breaking are for deep water or sloping beaches for which the process consists of steep wave formation, overturning jet and first plunge, followed by repeated forward splashups and plunges of decreasing scales. Early experiments are focused on geometric properties [1], wave breaking process [2], energy dissipation [3], jet characteristics and air entrainment [4], and turbulence [5]. More recent studies using PIV provide more detailed velocity, turbulence, and void fraction data and analysis [6-9]. Early CFD is 2D and focused on the wave breaking process and velocity [10-11]. More recent CFD is 3D and includes discussion of air entrainment, 2D and 3D vortex structures, and energy dissipation [12-13]. Often the experiments guide analysis of the CFD; however, in most cases CFD geometry and conditions differ from the experiments.

Present interest is ship hydrodynamics for which body-wave interactions are important and the direction of wave breaking is opposite to the mean flow. Previous research used model ships in towing tanks focused on scars, vortices and mean and rms wave elevation induced by ship bow and shoulder wave breaking [14-16], which suggests the presence of underlying coherent structures. The latter study included complementary CFD [17]. However, detailed measurements of the wave breaking processes are difficult using model ships in towing tanks. Recently, Shakeri et al. [18] provide detailed measurements and analysis of divergent bow waves using a unique wave maker for simulating 2D+t flow. For slender bow ships, 2D+t wave breaking process is similar to deep water and sloping beach studies, i.e., plunges with forward splashups.

The objectives of the present complementary experimental and CFD research are to provide a detailed description of plunging wave-breaking processes including wave-body interactions and wave breaking direction opposite to the mean flow, and provide benchmark data for CFD validation by using

[1]**Current affiliation:** Institute of Marine Industry, Gyeongsang National University, South Korea

the building block model and conditions of impulsive flow over a bump in a shallow water flume. The focus is on large-scale organized oscillations appropriate for development/validation of two-phase flow CFD similarly as done previously for single-phase flow CFD [19] using the experiments of a surface-piecing NACA 0024 foil [20]. The results are compared with the previous experimental and computational studies.

EXPERIMENTAL METHODS

The Iafrati et al. [21] quadratic profile bump is mounted in a shallow water flume for impulsive sub critical flow conditions such that a plunging breaking wave occurs downstream of the bump above a region of flow separation. Phase averaged measurements (relative to the time at which the maximum wave height is reached just before the first plunge) are conducted: (1) wave gauge water elevations upstream and downstream; (2) pitot velocities upstream and downstream; (3) venturi meter flow rates; (4) 2D PIV or video wave breaking profiles at maximum height just before the first plunge; (5) 2D PIV center-plane velocities and turbulence upstream and inside the plunging breaking wave; and (6) bottom pressures under the breaking wave.

Each plunging wave breaking experiment consists of J individual tests used for the phase averaging. The experiment was conducted ten times. Initially, Ghosh [22] conducted seven experiments with J = 22, but with limited documentation of the overall flume flow. Experiments L1-L3 are for PIV with large field of view. Experiments S1-S3 are for PIV with small field of view. Experiment V1 is for upstream PIV and limited overall flume flow. Subsequently, Reins [23] conducted three more experiments L4, S4, V2 with J = 24 and improved individual test repeatability and extensive documentation of the overall flume flow.

The experiments were conducted in the IIHR 30.0 m long, 0.91 m wide and 0.45 m deep re-circulating flume. The bump is mounted to the flume floor 17.29 m from the headbox. A Cartesian coordinate system is used for the measurements with x = 0 at the bump maximum height H with x > 0 pointed downstream, y = 0 at the flume/bump centerplane, and z = 0 at the flume/bump bottom with z > 0 pointed upwards. The coordinates (x, y, z) and water elevations ζ are non-dimensional using H. The bump profile z_B is

$$z_B(x) = 1 - 2x^2 / L^2 + x^4 / L^4 \qquad (1)$$

L=2.5 is the bump half-length.

A bump height H = 0.1143 m, initial water depth ζ = 2 (aspect ratio = 5.0), and pump frequency of 55 Hz in 7 s for Ghosh [22] and 40 Hz in 7 s for Reins [23] are used, which generates an impulsive plunging breaking wave with maximum wave height of about 12 cm with relatively small side disturbances. The wave breaking time t_b, i.e., the time at which the maximum height is reached just before the first plunge is used for phase averaging. An individual test is considered acceptable if the maximum height (x_b, z_b) is within a box of (X_b, Z_b) where (X_b, Z_b) = (3.12,1.98) for Ghosh [22] and (X_b, Z_b) = (3.14,2.15) for Reins [23]. Reins [23] reduced the pump frequency from 55 Hz to 40 Hz for improved repeatability of individual tests, which is the reason for the differences in X_b and especially Z_b values. In general, one in three individual tests was deemed acceptable. Unacceptable tests were due to side disturbances. Overhead video images were used to document the two-dimensionality of the plunging wave breaking. At maximum wave height just before the first plunge, the region $y = \pm 2.1$(54%W where W is the flume width) is approximately 2D, whereas close to the walls the wave profile is disturbed/broken. At the first plunge, the center 2D region increases to 60%W.

Data reductions equations are derived for the i^{th} time of the j^{th} test t_{ij} referenced to the breaking time t_{bj} and phase averaged water elevations, upstream and downstream axial velocity, 2D PIV axial and vertical velocities and Reynolds stresses under the breaking wave, and bottom pressures under the plunging breaking wave. Water elevations were measured using four Kenek servo-type needlepoint wave gauges. United Sensor pitot probes were used. Two venturi meters located within the re-circulation pipes are used to calculate the instantaneous flow rate. PIV measurements were made using a LaVision 2D system. Pressure taps are connected to pressure transducers. Data acquisition uses two synchronized PCs. PC1 uses a data acquisition board with LabView for acquisition of analog data for water elevations, pitot axial velocities, ventrui flow rates, and bottom pressures. PC1 triggers PC2 using the wave elevation at x = -7.5. When the water elevation drops by a specified amount $\Delta\zeta$ the LabView program sends a 5 Volt square sine wave to PC2. The initial condition for all tests was ζ = 2. The pumps were primed and the water elevation was calm, which required 30 minutes between individual tests. The tests were initiated by turning on the pumps and starting the PC1 LabView data acquisition. Ghosh [22] triggered PC1 using the criteria $\Delta\zeta$=-0.0175 at x=-62; however, this did not provide as accurate estimate of the time difference between the start of the pumps and PC1 data acquisition. Reins [23] manually started PC1 just after turning on the pumps with a difference of less than .1 s, which was corrected using the ventrui meter flow rate measurements. Convergence studies were conducted to determine the number of individual tests required for the phase averaging. The uncertainty analysis follows ASME [24] procedures. Kang et al. [25] provides a detailed description of the experimental methods and overall results.

COMPUTATIONAL METHODS

CFDShip-Iowa version 6, a sharp interface Cartesian grid solver for two-phase incompressible flows recently developed at IIHR by Yang and Stern [26], is used for the computational study. In this solver, the interface is represented by the level set (LS) method, which was later extended by Wang et al. [27]

using a coupled level set and volume-of-fluid (CLSVOF) method. A ghost fluid methodology is adopted to handle the jump conditions across the interface, where the density and surface tension effect are treated in a sharp way while the viscosity is smeared by a smoothed Heaviside function. A sharp embedded boundary method is used to handle complex immersed boundaries on Cartesian grids.

Mathematical Model

For the incompressible viscous flows of two immiscible fluids with constant properties, the Navier-Stokes equations are given by

$$\frac{\partial \mathbf{u}}{\partial t} + \mathbf{u}\cdot\nabla\mathbf{u} = \frac{1}{\rho}\nabla\cdot\left(-p\mathbf{I} + \mathbf{T}\right) + \mathbf{g} \tag{2}$$

$$\nabla\cdot\mathbf{u} = 0 \tag{3}$$

where t is time, $\mathbf{u}$ is the velocity vector, p is pressure, $\mathbf{I}$ is the unit diagonal tensor, ρ is density, $\mathbf{g}$ represents the acceleration due to gravity, and $\mathbf{T}$ is the viscous stress tensor defined as

$$\mathbf{T} = 2\mu\mathbf{S} \tag{4}$$

with μ the dynamic viscosity and $\mathbf{S}$ the strain rate

$$\mathbf{S} = \frac{1}{2}\left[\nabla\mathbf{u} + \left(\nabla\mathbf{u}\right)^{T}\right] \tag{5}$$

where the superscript $\mathbf{T}$ represents transpose operation. Density and viscosity are discontinuous across the interface, which is a function of time and space. They will be defined using the LS function later.

Since the fluids considered here are viscous and no phase change occurs, the velocity across the interface Γ is continuous:

$$[\mathbf{u}] = 0 \tag{6}$$

where [ ] denotes the jump at the interface, i.e., $[f] = f_L^I - f_G^I$ for a variable f with superscript I representing interface. Surface tension force is neglected.

A coupled level set and volume-of-fluid (CLSVOF) method [27] is used to capture the water/air interface where the interface is represented by the LS function and mass conservation is enforced with the VOF function. The LS function, ϕ, is defined as a distance function which is negative in the air, positive in the liquid, and zero at the interface. The VOF function, F, is defined as the liquid volume fraction in a cell with its value in between zero and one in a surface cell and zero and one in air and liquid respectively.

The LS function and the VOF function are advanced by the following equations, respectively,

$$\frac{D\phi}{Dt} = \frac{\partial\phi}{\partial t} + (\mathbf{u}\cdot\nabla)\phi = 0 \tag{9}$$

$$\frac{DF}{Dt} = \frac{\partial F}{\partial t} + (\mathbf{u}\cdot\nabla)F = 0 \tag{10}$$

The LS advection equation is solved using the third-order TVD Runge-Kutta scheme [28] for time advancement and the fifth-order HJ-WENO scheme [29] for spatial discretization. It should be noted that since the VOF function is not smoothly distributed at the free surface, an interface reconstruction procedure is required to evaluate the VOF flux across a surface cell. Finally, in order to achieve mass conservation, the LS functions have to be re-distanced prior to being used.

Each phase of constant density and viscosity can be defined using the LS function in the computational domain and sharp jumps of the fluid properties occur at the phase interface. In this study, the density keeps its sharp jump and the viscosity is smoothed over a transition band across the interface,

$$\begin{aligned}\rho &= \rho_G + (\rho_L - \rho_G)\,H(\phi)\\ \mu &= \mu_G + (\mu_L - \mu_G)\,H_\varepsilon(\phi)\end{aligned} \tag{11}$$

where the subscripts G and L represent gas and liquid phase, respectively, the stepwise Heaviside function is

$$H(\phi) = \begin{cases} 1 & \text{if} \quad \phi \geq 0 \\ 0 & \text{if} \quad \phi < 0 \end{cases} \tag{12}$$

and the smoothed Heaviside function is

$$H_\varepsilon(\phi) = \begin{cases} 1 & \text{if} \quad \phi > \varepsilon \\ \frac{1}{2}\left[1 + \frac{\phi}{\varepsilon} + \frac{1}{\pi}\sin\left(\frac{\pi\phi}{\varepsilon}\right)\right] & \text{if} \quad |\phi| \leq \varepsilon \\ 0 & \text{if} \quad \phi < -\varepsilon \end{cases} \tag{13}$$

Numerical Method

The flow equations are discretized on a staggered Cartesian grid with the convection terms approximated by a third-order QUICK scheme [30] and other terms by the standard second-order central difference scheme. A semi-implicit time-advancement scheme is adopted to integrate the momentum equations with the second-order Crank-Nicolson scheme for the diagonal viscous terms and the second-order Adams-Bashforth scheme for the convective terms and other viscous terms. A four-step fractional-step method is employed for velocity-pressure coupling. The resulting pressure Poisson equation is solved using the PETSc library [31]. Details of the numerical methods can be found in the studies by Yang and Stern [26].

A sharp interface immersed boundary method is adopted here to treat the immersed boundaries/bodies in a non-uniform Cartesian grid. In this approach, the grid generation for

complex geometries is trivial since the requirement that the grid points coincide with the boundary, which is imperative for body-fitted methods, is relaxed; while the solution near the immersed boundary is reconstructed using momentum forcing in a sharp-interface manner.

Code Architecture and HPC

One of the major objectives of the development of CFDShip-Iowa version 6 is to make use of the on-coming petascale computers and provide fast turnaround for simulation-based design in ship hydrodynamics. Efficiency and sustainable development of the solver are among the major considerations in the software design.

The parallelization is done via a domain decomposition technique using the MPI library. A simple domain decomposition technique is used in CFDShip-Iowa version 6 where the Cartesian grid is divided into uniform pieces, each of which resides in one processor. Optimal load balance can be achieved except for a small amount of overhead due to interface and immersed boundary treatment, which may be unevenly distributed over processors.

A parallel tri-diagonal system solver is used with the approximate factorization of momentum equations, no iterations are needed for the inversion of the momentum equations. For the pressure Poisson equation, a highly efficient, scalable multigrid-preconditioned Krylov subspace solver from PETSc has been included in the code. Usually, the Poisson solver takes most of the CPU time in a single time step.

Computational Setup

The 2D simulations are conducted on a computational domain of x = [-52, 44] and z = [0, 5]. Four different grids are used in the simulations, as shown in Table 1. The grid G0 (768×256) has 48 more points in the z direction than the coarse grid (G3) and has similar plunging wave breaking positions as the medium grid (G2). Grids (G1, G2, G3) are systematic with consecutively reduced (by a factor of 2) sizes from 3072×832 to 1536×416 and 768×208 and used for a grid convergence study. The medium grid results are presented and the fine grid simulations are in progress. The computational domain and boundary conditions are given in Fig. 1. The time-dependent velocity and wave elevation boundary conditions are specified at the inlet and outlet using the exact experimental data [23] as shown in Fig. 2. The computation is started with both water and air at rest. In the present simulation, a constant CFL number of 0.2 is used where the magnitude of the time step varies from 1×10^{-2} to 1×10^{-5} depending on the flow conditions.

Verification and Validation

Wave breaking time (t_b) and positions (x_b, z_b) on the four different grids are shown in Table 1. Verification is conducted following the FS method [32-33], as shown in Table 2. Monotonic convergence is observed for t_b, x_b, and z_b with convergence ratio (R_G) 0.11, 0.67, and 0.66, respectively. Small grid uncertainty is obtained for t_b, whereas relatively large grid uncertainty is shown for x_b and z_b.

Figure 3 (c) shows the wave profiles at t_b for all four grids. As the grid is refined, t_b and x_b are closer to the experimental results and errors are reduced to 1.26% and 0.3%, respectively, as shown in Table 1. However, z_b from the fine grid has the largest error compared to the other two grids.

OVERVIEW OF THE EXPERIMENTAL AND COMPUTATIONAL RESULTS

Experimental Results

A total number of 226 individual plunging wave-breaking tests were conducted. Each test followed a similar time line. The plunging wave breaking experiment takes about Δt_T=22.9 s and can be decomposed into four time phases: startup $-13.4 \le t \le -.9$ s (Δt_S=12.5 s =54.6%Δt_T); steep wave formation $-.9 \le t \le 0.0$ s (Δt_{SWF}=0.9 s =3.9%Δt_T); plunging wave breaking $0.0 \le t \le 1.4$ s (Δt_{PWB}=1.4 s =6.1%Δt_T); and chaotic wave breaking swept downstream $1.4 \le t \le 9.5$ s (Δt_{CWB}=8.1 s =35.4%Δt_T).

The startup from the static condition is initiated by simultaneously turning on the pumps and starting the PC1 data acquisition. The downstream water at x=44 goes into motion first, whereas the upstream water at x=-52 goes into motion subsequently at t=-6 s. The acceleration of the water in the flume induces a shallow-water wave η, which initiates at t=-9.75 s. A bump vortex is formed.

During steep wave formation the plunging wave breaking forms downstream on top of the separation region of the bump reaching maximum height x_b=3.45 and z_b=2.14 at t=0 s, as shown in Fig. 3. At t=0 s, η is at x=18; the region of separation is shed downstream below the bump vortex center at x_{BV}=4.6 and z_{BV}=1.2.

The plunging wave breaking process consists of four repeated plunging events each with three [jet impact (plunge), oblique splash and vertical jet] sub-events, which were identified using the complementary CFD [27]. The first and second plunges take the longest 38.1%Δt_{PWB} and 23.9%Δt_{PWB}, respectively, whereas the last two plunges take 19%Δt_{PWB} and 19.1%Δt_{PWB}, respectively. Oblique splashes and vertical jets account for 23.8%Δt_{PWB} and 66.7%Δt_{PWB}, respectively, i.e., more time is spent splashing than plunging. The flume acceleration wave η travels to x=44 at t=1.53 s with average amplitude .28 and speed 2.8 m/s. The bump vortex center is at x_{BV}=4.8 and z_{BV}=1.2 at t=.2 s after which it exits the large field of view PIV measurement area. The wave breaking vortex center travels from x_{WBV}=3 and z_{WBV}=.95 at t=.4 s to x_{WBV}=3.8 and z_{WBV}=.7 at t=.675 s. Figure 4 shows the time history of the bump vortex, wave breaking vortex and n=1−4 plunging entrapped air bubble (x_{An},z_{An}) trajectories and entrapped air bubble diameters (D_{An}).

After the fourth plunge-oblique splash-vertical jet event, chaotic splashing occurs, which is swept downstream beginning at about t=1.67 s and reaches x=8 at t=7 s after which an hydraulic jump is formed with water elevation ζ^8=.6 until the end of the experiment. At t=9.5 s, the pumps are turned off and the data acquisition is stopped.

The wave breaking times t_b and maximum height positions (x_b, z_b) are similar for both sets of experiments with standard deviation 1.53%T_b (.2 s) for Gosh [22] and 2.1%T_b (.28 s) for Reins [23]. Overall average (x_b, z_b) positions are (3.26,1.88) for Ghosh [22] and (3.45,2.14) for Reins [23]. The axial and vertical positions are, respectively, 3% and 13% larger for Reins [23] than Ghosh [22]. Figure 3a compares the average wave breaking profiles for experiments L1-4 and S1-4, including Ghosh [22] and Reins [23] acceptability boxes $\pm 6\%(x_b, z_b)$.

Reins [23] compared his extensive documentation of the overall flume flow with the limited documentation provided by Ghosh [22]. Water elevations, upstream and downstream velocities, and venturi meter flow rates are qualitatively similar, but the standard deviations for Ghosh [22] are nearly an order of magnitude larger than Reins [23]. The upstream velocities were smaller and downstream velocities larger for Ghosh [22] than Reins [23], but the average axial PIV velocities under the breaking wave at t_b are similar, i.e., about 0.6 m/s. PIV movies of axial and vertical velocities, Reynolds stresses, TKE, and transverse vorticity for L1-4 and S1-4 are qualitatively and quantitatively similar. Therefore, in spite of the aforementioned differences, all ten experiments are considered multiple realizations of the same plunging wave breaking process. Reins [23] standard deviations are smaller than Ghosh [22] for most measurements indicating improved repeatability, which is attributed to reducing the pump frequency from 55 to 40 Hz. In addition, Reins [23] provides extensive documentation of the overall flume flow compared to Ghosh [22]; thus, the following presentation of flume flow, plunging wave breaking, and bottom pressure focus on the L4, S4, and V2 results.

CFD Results

Initially, Huang et al. [34] used the Ifarati et al. [21] bump and conditions as a numerical benchmark in the development of their coupled ghost fluid/two-phase level set method for curvilinear body-fitted grids. These results were used as a guide for the test design of the present experiments and the initial experimental data was used for validation.

Subsequently, complementary CFD was used to aid in the data analysis simultaneously as the experimental data is used to validate a Cartesian grid, immersed boundary, coupled level set and volume-of-fluid CFD method [27]. Wang et al. [27] indentified three repeated plunging events each with three sub-events; however, they used fully impulsive initial conditions and adjusted the initial velocity and water elevation to match Ghosh's [22] (x_b, z_b) values, which precluded detailed spatial and temporal validation.

Present CFD uses the exact experimental initial and boundary conditions. The simulations predict the same four time phases and four repeated plunging events as the experiments, but are thus far terminated at t = 1.99 s. The wave breaking time and maximum height are accurately predicted but the axial distance is 26%x_b downstream, as shown in Fig 3a. This discrepancy is attributed to use of a medium grid that under resolves the bump boundary layer and region of separation. Thus, to facilitate the comparisons the simulation results were translated axially for the same x_b at t_b, as also shown in Fig 3a. The shape of the predicted wave profile is similar to the experiments.

Tables 3 and 4 provide the percentage of the plunging wave breaking time phases for the experiments and simulations, respectively, truncated at the end of the plunging wave breaking phase to facilitate the comparisons such that Δt_T = 14.8 s for the experiments and 15.76 s for the simulations. The combination of the startup and steep wave formation phases are 90.5 and 87.3%Δt_T, respectively for the experiments and simulations. The differences in t_b between the experiments and simulations are only .37 s. However, the plunging wave breaking phase is .59 s longer for the simulations than the experiments such that Δt_{PWB} = 9.5 and 12.6%Δt_T, respectively for the experiments and simulations. The average plunging event time interval is .35 s for the experiments and .5 s for the simulations. The second and third plunges take the longest followed by the first and last. Oblique splashes and vertical jets account for 9.5%Δt_{PWB} and 17.5%Δt_{PWB}, respectively, i.e., more time is spent in plunging than splashing, which is opposite to the experiment. Table 5 shows time interval of each plunging phase. Grid G0 and G2 spend longer time on the second plunge than other plunging phases, while EFD and G3 show the first plunge takes longer than other phases.

The simulations accurately predict the flume acceleration wave, as will be shown later. The simulations predict the bump and wave breaking vortex trajectory trends, but with some differences, as shown in Fig. 4.

FLUME FLOW

Experimental Results

The overall flume flow was documented by measurements of water elevations from upstream to downstream of the bump; upstream and downstream pitot velocities; upstream PIV; and venturi meter flow rates.

Figure 5 shows the time history of the water elevation. The most downstream measured water elevation at x=70 decreases beginning at t=-11 s. The most upstream measured water elevation at x=99 increases beginning at t=-9 s. The upstream water elevation increase is due to a flume acceleration wave η that travels down the flume with average height $\Delta\zeta$=.4 and speed 1.9 m/s. The wave is visible in the time histories of the water elevations. At t=0 s, η is downstream of the plunging wave breaking at x= 18. Downstream wave heights are smaller

than upstream. For x<0, after the wave passes each measurement location the water elevation remains elevated at about $\Delta\zeta$. For x=0, after the wave passes the water elevation returns to the initial water elevation ζ=2. For x=8, after the wave passes (t=-.5 s) the water elevation decreases until t=7 s after which it remains constant at ζ=.5. For t>1.67 s, the plunging breaking wave is swept downstream creating a hydraulic jump, which reaches x=8 at t=7 s. For x>8, after the wave passes each measurement location the water elevations remain constant at ζ=1.6, 1.5, 1.4, and 1 for x=18, 31, 44, and 70, respectively.

Figure 6 shows the time history of the flume-acceleration wave η location, amplitude and speed. The location was defined as the time when half the wave height passes the measurement location. The wave speed is approximately constant with average 1.93 m/s. The wave heights are larger upstream than downstream of the bump with average $\Delta\zeta$=.37. The small amplitude shallow-water/stationary wave speed estimate is $\sqrt{g\varsigma} = 1.5$ m/s. Figure 6 includes the finite amplitude shallow-water/stationary wave speed estimates $\sqrt{g\varsigma}\ 1+\Delta\varsigma\ ^{1/2}$ for comparison, which has the value 1.8 m/s using the average $\Delta\zeta$.

The upstream velocity initially increases rapidly then gradually reaching a maximum of 0.55 m/s at t =4.45 s after which it remains nearly constant for t>7 s, as shown in Fig. 2. At t=-4 s (transitional flow condition), the Re^u=59,450, which is much larger than typical transition Re for fully developed open channel flow, due to flow acceleration. The maximum Re^{umax}=143,750 and Fr^{umax}=.4 occur at t=3 s. The upstream PIV velocities are zero for t=-11,-9, and -7 s. For t=-5, the profile is laminar. For t=-4 s, the profile is transitional. For t=-3, -1, 0, 1, and 3 the profile is turbulent with overshoots. For t=5 s and 7 s, the profile is decelerating and especially retarded in inner region.

The downstream velocity increases gradually to .8 m/s at t=1.56 s followed by rapid increase to 1.125 m/s and remaining at this value for t>4.76 s. At t=-5 s, Re^d=50,000 and Fr^d=.25. At t=-1.33 s, Re^d=75,000 and Fr^d=.425. At t=0 s, Re^d=80,000 and Fr^d=.5. At t=3 s, Re^d=150,000 and Fr^d=.875 reach their maximum values and remain approximately constant until the end of the experiment.

CFD Results

The simulations accurately predict the water elevations including the flume acceleration wave, as also shown in Figs. 5 and 6. Note that the present simulations used the exact experimental upstream and downstream velocity and water elevation as initial and boundary conditions; however, for laminar flow, i.e., a turbulence model was not used.

PLUNGING WAVE BREAKING AND BOTTOM PRESSURE

The major events of the plunging wave breaking process are shown in Fig. 7, including the video images, PIV image with overlaid CFD wave profile, *U* and *W* velocity contours from both experiments and CFD. Fig. 8 shows wave breaking energies averaged over the PIV field of view. Bottom pressure variations with time are given in Figs. 9 and 10.

Experimental Results

The first plunging event and sub-events are displayed in Fig. 7 using video images with red dye (VR; Reins, [23]) and L4 PIV raw images and $\langle U_i \rangle$ and $\langle W_i \rangle$ contours with overlaid perturbation velocity vectors $<\Delta\underline{V}_i>$, including the corresponding simulation results for comparisons. Not shown are the other time phases and second through fourth plunging events and sub-events, video images without red dye (VG; Ghosh, [22]), $\sqrt{<TKE_i>}$, $\langle uw_i \rangle$ and S4 PIV. Since the breaking times and acquisition intervals are different for VG ($-0.667 \le t \le 1.53$ s), VR ($-1.33 \le t \le 1.67$ s), L4 ($-1.33 \le t \le 1.67$ s), and S4 ($-0.6 \le t \le 0.6$ s) they were phase aligned using t_b. VR was used to identify the times relative to t_b of the four repeated plunging events and their jet impact, oblique splash and vertical jet sub-events. VG, L4 and S4 are shown at the same times as VR assuming their events and sub-events times are approximately equal; however, this is a rough approximation since the standard deviation in breaking time is about .24s and the average time between breaking sub-events is about .14s. The plunging events and sub events are also evident in the instantaneous PIV images, but not as clear as in the VR images.

The VG video images visualize the steep wave formation and first plunge and oblique splash after which images show two-phase bubbly turbulent flow in the breaking region, which eventually is swept downstream. It is difficult to identify organized structures, although some of the vertical jet sub-events are apparent. The VR video images enable identification of the plunging wave breaking process, which as already described consists of four repeated plunging events each with three plunge, oblique splash, and vertical jet sub-events.

Near the end of the startup phase the water surface is flat, although η is visible at x=3. The axial velocity accelerates over the bump and separation region behind the bump. The vertical velocity is upward behind the bump and downward in the back of the separation region near x=3.5. The center of the bump vortex is at (x_{BV},z_{BV})=(2.9,.9) with maximum strength about 12 s^{-1} and diameter $0.32\zeta_0$. The turbulence levels are high near η and in the shear layer between the accelerated flow over and separated flow downstream of the bump.

Figure 7a is for t_b, i.e., maximum height ζ_{max}=2.14 at x=3.38. The face of the wave is broken and jet formation at the wave crest. The region of high axial velocity extends under the wave crest and pushes the separation region downstream; also high axial velocity on the backside of the wave. The vertical velocity is downward behind the bump and upward towards the wave crest. The center of the bump vortex is at (x_{BV},z_{BV})=(4.7,1.2). The $\sqrt{<TKE_i>}$ and $<uw_i>$ are largest on

the backside and face of the wave and the shear layer above the separation region.

Figure 3b compares the L4 and S4 wave breaking profiles with other studies using wave height H_w and length λ for scaling of z and x, respectively. The average H_w for the other experimental studies is .13 m, which is similar to L4/S4 H_w = .12/.13 m values. The λ values were estimated using the zero crossing method either twice trough to crest or trough to trough depending on the available data. For the other experimental studies, the λ values vary considerably $0.3 \le \lambda \le .8$ m such that wave steepness $0.45 \le ak \le 1.15$. For L4/S4 λ= .28/.23 m such that *ak*=1.35/1.79. For all studies the *ak* values are consistent with geometric breaking criteria for deep [35] and shallow [4] water. The wave faces for all studies have a similar shapes albeit with spreading, whereas the wave back shapes correlate with *ak* such that the smaller values are more symmetric and the larger values approach the horizontal similar to a tidal bore. The wave faces for all studies are much steeper than the limiting Stokes wave and nearly vertical near the crest. The wave backs for all studies are also much steeper than the limiting Stokes wave and approach the horizontal for large *ak* such that the wave asymmetry is largest for the steepest waves. Note that the average wave speed C for the other experimental studies is 1.5 m/s in the direction of wave breaking, whereas the average axial velocity at t_b for L4/S4 is .6 m/s in the opposite direction to the wave breaking.

Figure 7b is for the first plunge. The plunging jet shoots out from the wave face, falls, and touches the wave trough entraining air bubble A1. The jet angle is 48 deg, which is close to the average (51 deg) of the other experimental and computational studies. The jet velocity is -0.2 m/s, i.e., the relative velocity is -1.33 $\langle \bar{U}_b \rangle$. Chang et al. [36], Chen et al. [10], Perlin et al. [37], and Shakeri et al. [38] report jet relative velocities 0.5, 0.45, 0.3, and 0.18-0.2C, respectively. The jet thickness is $0.2H_w$, which is similar to Bonmarin [1], Grue et al. [6], Kimmoun et al. [7] value $0.14H_w$. The $\sqrt{< TKE_i >}$ is largest in the jet, on the wave face and back, and in the shear layer above the separation region. The $<uw_i>$ is largest in the jet and on the wave face and back. The shape of the first entrained air bubble is an ellipse with aspect ratio $\sqrt{3}$, as reported in most other studies. The air bubble diameter is $0.18H_w$, which is similar to Blenkinsopp and Chaplin [8], Chang et al. [36], Chen et al. [10], and Rapp and Melville [39] values 0.1, 0.34, 0.2, $0.24H_w$, respectively. The air bubble penetrates to $0.375<\zeta_0>$, which is similar to Blenkinsopp and Chaplin [8], Chanson et al. [4], Lubin et al. [13] values 0.19-0.28, 0.16-0.5, $0.4\text{-}0.6\zeta_0$, respectively. The air bubble speed is $\langle \bar{U}_b \rangle$ in the direction opposite to the wave breaking, whereas Chang et al. [5] report .55C in the direction of the wave breaking.

Figures 7c is for the first oblique splash. The plunging jet rebounds off the wave trough forming the oblique splash, which subsequently grows and fans out. The angle of the oblique splash is 35 deg, which is similar to the other experimental studies values 32-40 deg with 35 deg average value. The region of bubbly flow increases, as the wave crest plunges into the wave trough. The axial velocity increases and upward vertical velocity decreases. The turbulence is high in the breaking region. The center of the bump vortex is at $(x_{BV},z_{BV})=(4.74,1.15)$. A1 is at $(x_{A1},z_{A1})=(3.2,1.5)$.

Figure 7d is for the first vertical jet. VG shows large region of splashing and bubbly flow, which masks the organized structure of the vertical jet at $(x_{VJ1}, z_{VJ1})=(3.5, 2)=(103, 93)\%(x_b, z_b)$ and A1 at $(x_{A1}, z_{A1})=(4.2, 1)$ seen in VR. The wave crest is swept downstream at x=4. The wave breaking vortex is at $(x_{WBV},z_{WBV})=(3.5,.84)$. The $<uw_i>$ levels are at a maximum.

Figures 7e is for the second plunge. The locations of the second and third vertical jets are $(x_{VJ2}, z_{VJ2}) = (3.4, 1.8) = (100.5, 84)\%(x_b, z_b)$ and $(x_{VJ3}, z_{VJ3}) = (3.3, 1.7) = (96, 79)\%(x_b, z_b)$, respectively. The wave breaking vortex is at $(x_{WBV}, z_{WBV}) = (3.6, .71)$ and (3.7, .7) for second plunge and oblique splash, respectively, with maximum strength about –(7-10) s^{-1} and diameter $0.2\zeta_0$. The air bubble diameters and trajectories are evident, as summarized in Fig. 3b. The air bubble diameters and trajectories are estimated using VR by tracking the size of the two-phase region of entrapped air corresponding to each plunging event.

The other experimental and computational studies are for deep water or sloping beaches for which the process consists of steep wave formation, overturning jet and first plunge, followed by repeated forward splashups and plunges of decreasing scales. Blenkinsopp and Chaplin [8] and Chang et al. [5] report splashups with heights 1-1.2 and $0.55H_w$, respectively, and 1 air bubble. Chen et al. [10] results show maximum height followed by plunge, splashup, and plunge process with one entrapped air bubble. Kimmoun et al. [7] report two plunge/splashup cycles with decreasing splashup heights ($.85H_w$ for first and $.43H_w$ for second) and three air bubbles. Lubin et al. [13] results show three plunge/splashup cycles and three air bubbles. The penetration depth for the second air bubble is $0.2\text{-}0.45\zeta_0$, which is less that the value given previously for the first. Rapp and Melville [39] report plunge with spashups with maximum height $.73H_w$ and one air bubble. Tallent et al. [2] and Watanabe et al. [11] indicate plunges with several splashups and air bubbles.

The other experimental and computational studies show instantaneous and phase-averaged wave breaking vortices and turbulence. Instantaneous co-rotating vortices are observed during plunging and air entrainment [2, 10, 11, 13]. Melville et al. [38] observe a large phase-averaged vortex with rotation in the direction of wave breaking, speed 1% wave speed, strength .25-3.1 s^{-1}, and decays as t^{-1}. Chang et al. [5, 36], Kimmoun et al. [11], and Perlin et al. [37] report 6, 4, 25 and 20 s^{-1} vortex strengths, respectively.

Figure 8 shows the plunging wave breaking kinetic, potential, and total energy averaged over the PIV field of view. Not shown are the $\sqrt{< TKE_i >}$, $<uw_i>$, and spanwise vorticity

$< \omega_{y_i} >$. Prior to t_b the potential energy is much larger than the kinetic energy with maximum value at maximum height. Subsequently, the potential energy drops rapidly to about 40% of its maximum value with oscillations, whereas the kinetic energy continuously increases. The potential energy decays as $t^{-0.3}$. After the second plunge, the kinetic energy is larger than the potential energy. Thus, the total energy continuously increases reaching its maximum at t_b after which it drops with oscillations until the third plunge followed by oscillatory and continuous increase. The turbulence intensity is largest at t=-0.7 due to the turbulence in the separation shear layer downstream of the bump followed by fairly large (10% mean velocity) oscillatory decreasing as $t^{-0.3}$ values during the plunging wave breaking. The Reynolds shear stress shows large values during wave breaking. The spanwise vorticity shows large positive values prior to wave breaking due to the bump vortex and large negative values during wave breaking due to the wave-breaking vortex.

The other experimental and computational studies show alternating decreases/increases in potential/kinetic energy during plunge/splashup cycles [13]. Most of the energy is dissipated within the first several wave periods with decay as t^{-1} [5, 40] and as $t^{-0.3}$ [13]. Chang et al. [5], Rapp and Melville [39], and Watanabe et al. [11] report turbulence intensity about 10, 2, and 8 % wave speed, respectively. Melville et al. [40] report TKE and Reynolds stress decay t^{-1}. Drazen et al.[9] report TKE decay as $t^{-0.75}$.

Figure 9 shows the bottom pressure $<P_i>$ measurements for L4 and S4. Initially $<P_i>$=1.0 since it is normalized by ρg2H, i.e., the initial water depth hydrostatic pressure. For $t \le t_b$, $<P_i>$ follows the potential energy. For $t>t_b$, $<P_i>$ decreases with oscillations during the plunging wave breaking process. The pressure head normalized by H ($=2\rho g<P_i>$) at the same times as Fig. 7 with overlaid PIV images and perturbation velocity vectors colored by velocity magnitude shows that for $t < t_b$ the pressure head coincides with the water elevation, whereas for $t \ge t_b$ the pressure head is in the two-phase flow region.

CFD Results

The simulations qualitatively predict the same four time phases as the experiments, but with different percentages of the total time, as already discussed. The startup phase is .32 s longer, the steep wave formation phase is .05 s longer, and the plunging wave phase is .59 s longer than the experiments such that the first three phases are .96 s longer for the simulations than the experiments. The experimental trends are exhibited by the simulations, but generally with reduced axial and vertical velocity magnitudes, as shown in Fig. 7. As already discussed, the simulations over predict x_b by 26%; however, the wave breaking profile is close to the experiment and similarly scales with the other studies, as shown in Fig 3. The wave height, length and steepness for the simulations are 0.1 m, 0.2 m, and 1.57, respectively. The first plunge jet angle, speed, and thickness are 42 deg, -.4 m/s, and $.15H_w$. The shape of the first entrained air bubble is an ellipse with aspect ratio 2.1. The four entrapped air bubble speeds, diameters and penetration depths are (0.7,0.53,0.45,0.76) m/s, $(0.55,0.26,0.7,0.25)H_w$, and $(0.15,0.01,0.17,0.13)\zeta_0$, which are of similar magnitudes as the experiment, as shown in Fig. 4. The angle of the first oblique splash is 30 deg. The axial location and height of the four vertical jets are (2.6,2.2,3.1,2.4) and $(1.8,1.5,N/A,1.9)H_w$. The bump vortex has maximum strength about 10 s^{-1} and diameter $0.45\zeta_0$. The kinetic energy is over predicted for $t_b<0$, the potential energy is over predicted for $t_b>0$ such that the total energy is over predicted, as shown in Fig. 8.

The simulations show similar bottom pressure magnitudes, but with fairly large oscillations, which correlate with the plunging wave breaking events and sub-events. As shown in Figure 10, pressure peaks are corresponding to the locations where water height increases. When the first plunge occurs pressure increases at the plunge point and decreases at the points downstream. After the first plunge, pressure decreases at most points; and the oblique splash occurs as the pressure drops. The vertical jet is formed at the location where the pressure increases again. As the vertical jet decreases in height, the overall pressure at most positions drops. Same pressure patterns are shown in the repeated processes.

CONCLUSIONS

The plunging wave-breaking process for impulsive flow over a bump in a shallow water flume is described using complementary experiments and simulations. The geometry and conditions are relevant to ship hydrodynamics since it includes effects of wave-body interactions and wave breaking direction is opposite to the mean flow. Phase averaged measurements (relative to the time at which the maximum wave height is reached just before the first plunge) are conducted. Complementary CFD was used to guide the experiments, as the experiments were used to validate the CFD.

A total number of 226 individual plunging wave-breaking tests were conducted, which all followed a similar time line consisting of startup, steep wave formation, plunging wave breaking, and chaotic wave breaking swept downstream time phases. The overall flume flow was documented by measurements of water elevations from upstream to downstream of the bump; upstream and downstream pitot velocities; upstream PIV; and venturi meter flow rates.

The plunging wave breaking process consists of four repeated plunging events each with three [jet impact (plunge), oblique splash and vertical jet] sub-events, which were first identified using the complementary CFD by Wang et al. [27]. Video images with red dye display the plunging wave breaking events and sub-events. The first and second plunges take longer than the last two plunges. Oblique splashes and vertical jets account for more time than plunging. The wave profile at maximum height, first plunge, bump and wave breaking vortex

and entrapped air bubble trajectories, entrapped air bubble diameters, kinetic, potential, and total energy, and bottom pressures are analyzed. The present results suggest that repeated plunging events and sub-events may underlie the scars, vortices and mean and rms wave elevation observed for ship bow and shoulder wave breaking.

The simulations qualitatively predict all four time phases, all four plunging events and their sub-events, and bottom pressure but with reduced velocity magnitudes and larger post-breaking water elevations.

The present results show differences and similarities with other experimental and computational studies for deep water and sloping beaches. In particular, the breaking processes show differences due to the differences in mean flow direction. In the present study where the breaking is opposite to the mean flow, the breaking events involve repeated plunge, oblique splash, vertical jet, air-bubble entrainment sub events near the first plunge. In the other studies, the breaking is in the direction of the mean flow such that the breaking events involve repeated plunge/forward splashups and air-bubble entrainment sub events. Both show smaller scales as the plunging wave breaking repeated sub events dissipate into chaotic wave breaking. The present wave breaking profile is similar to those for very steep waves. The present results involve wave-body interactions due to the separated flow and bump vortex downstream of the bump. Nonetheless, many variables are similar for the present and other studies, including wave height, length, and steepness; jet angle, speed, and thickness; air bubble shape and size; splash angle and height; wave breaking vortex size and strength; potential energy dissipation; and turbulence intensity.

The experiment provides benchmark validation data for two-phase flow CFD for ship hydrodynamics building block geometry. The initial CFD used fully impulsive initial conditions, which precluded temporal validation. Present CFD is using experimental upstream and downstream conditions for more detailed and temporal validation. Four different grids are used in the present simulations. Solutions are sensitive to the grids; however, all the grids show all the plunging wave breaking features. In the present study, the medium grid results are presented. The fine grid simulations are in progress and the preliminary results are promising. In order to increase grid resolution near the bump, an orthogonal curvilinear grid solver will be used. The CFD will be used to guide future 3D experiments to document span-wise instabilities and vortex and turbulent structures.

ACKNOWLEDGMENTS

The US Office of Naval Research sponsored this research through grants N00014-01-1-0073 and N00014-06-1-0420 under the administration of Dr. Patrick Purtell. Dr. Suak-Ho Van contributed to the early stages of the experiments.

REFERENCES

[1] Bonmarin, P., 1989, "Geometric Properties of Deep-Water Breaking Waves," J. Fluid Mech. 209**,** pp. 405-433.

[2] Tallent, J.R., Yamashita, T., Tsuchiya, Y., 1990, "Transformation Characteristics of Breaking Water Waves," Water Wave Kinematics, pp.509-523.

[3] Melville, W. K., 1994, "Energy Dissipation by Breaking Waves." J. Phys. Oceanog., 24, pp. 2041-2049.

[4] Chanson, H., Fang L., 1997, "Plunging Jet Characteristics of Plunging Breakers." Coastal Enging., 31, pp. 125-141.

[5] Chang, K. A. & Liu, P. L. F., 1999, "Experimental Investigation of Turbulence Generated by Breaking Waves in Water of Intermediate Depth," Phys. Fluids, 11(11), pp. 3390-3400.

[6] Grue, J., Jensen, A., 2006, "Experimental Velocities and Accelerations in very Steep Wave Events in Deep Water," Euro. J. Mech. B/Fluids., 25, pp. 554-564.

[7] Kimmoun, O. and Branger, H., 2007, "A Particle Image Velocimety Investigation on Laboratory Surf-Zone Breaking Waves over a Sloping Beach," J. Fluid Mech., 588, pp. 353-397.

[8] Blenkinsopp, C. E., and Chaplin, J. R., 2007, "Void Fraction Measurements in Breaking Waves," Proc. R. Soc. A, 463, pp. 3151-3170.

[9] Drazen, D. A. and Melville, W. K., 2009, "Turbulence and Mixing in Unsteady Breaking Surface Waves," J. Fluid Mech., 628, pp. 385-119.

[10] Chen, G., Kharif, C., Zaleski, S., Li J., 1999, "Two-Dimensional Navier-Stokes Simulation of Breaking Waves," Phy.s Fluids, 11 (1), pp. 121-133.

[11] Watanabe, Y. and Saeki, H., 2002, "Velocity Field after Wave Breaking," Int. J. Numer. Meth. Fluids *3*9, pp. 607-637.

[12] Watanabe, Y., Saeki, H., Hosking, R., 2005, "Three-Dimensional Vortex Structures under Breaking Waves," J. Fluid Mech., 545, pp. 291-328.

[13] Lubin, P., Vincent, S., Abadie, S., Caltagirone, J. P., 2006, "Three-Dimensional Large Eddy Simulation of Air Entrainment under Plunging Breaking Waves," Coastal Enging., 53, pp. 631-655.

[14] Miyata, H. and Inui, T., 1984, "Nonlinear Ship Waves," Adv. Appl. Mech., 24, pp. 215-288.

[15] Dong, R. R., Katz, J. and Huang, T. T., 1997, "On the Structure of Bow Waves on a Ship Model," J. Fluid Mech., 346, pp. 77-115.

[16] Olivieri, A., Pistani, F., Wilson, R., Campana, E. F., and Stern, F., 2007, "Scars and Vortices Induced by Ship Bow and Shoulder Wave Breaking," J. Fluids Engng., 129(11), pp. 1445-1459.

[17] Wilson, R. V., Carrica, P. M., Stern, F., 2007, "Simulation of a Ship Breaking Bow Wave and Induced Vortices and Scars," Int. J. Numer. Meth. Fluids, 54, pp. 419-451.

[18] Shakeri, M., Tavakolinejad, M., and Duncan, J. H., 2009, "An Experimental Investigation of Divergent Bow Waves Simulated by a Two-Dimensional plus Temporal Wave Marker Technique," J. Fluid Mech., 634, pp. 217-243.

[19] Xing, T., Kandasamy, M., and Stern, F., 2007, "Unsteady Free-Surface Wave-induced Separation: Analysis of Turbulent

Structures using Detached Eddy Simulation and Single-Phase Level Set," J. Tur., 8(44), pp. 1-35.
[20] Metcalf, B., Longo, J., Ghosh, G., and Stern, F., 2006, "Unsteady Free-Surface Wave-Induced Boundary Layer Separation for a Surface-Piercing NACA 0024 foil: Towing Tank Experiments," J. Fluids & Struc., 22(1), pp. 77-98.
[21] Iafrati, A., Di Mascio, A., Campana, E. F., 2001, "A Level Set Technique Applied to Unsteady Free Surface Flows," Int. J. Numer. Meth. Fluids, *35*, pp. 281-297.
[22] Ghosh, S., 2008, "Free Surface Instabilities and Plunging Breaking Wave Downstream of a Bump in Shallow Water Open Channel Flume," Ph.D. thesis, the University of Iowa, USA.
[23] Reins, G., 2008, "Experimental Study of an Impulsive Plunging Breaker Downstream of a Bump in a Shallow Water Open Channel Flume," Master's thesis, the University of Iowa, USA.
[24] ASME, 2005. "Test Uncertainty," ASME PTC 19.1-2005. The American Society of Mechanical Engineers.
[25] Kang, D., Ghosh, S., Reins, G., Koo, B., and Stern, F., 2010, "Impulsive Plunging Wave Breaking Downstream of a Bump in a Shallow Water Flume," IIHR Report (in preparation), Iowa Institute of Hydraulic Research, The University of Iowa, Iowa City, Iowa, USA.
[26] Yang, J. and Stern, F., 2009, "Sharp Interface Immersed-Boundary/Level-Set Method for Wave-Body Interactions," J. Comput. Phys., 228(17), pp. 6590-6616.
[27] Wang, Z., Yang, J., Koo, B. G., and Stern, F., 2009, "A Coupled Level Set and Volume-of-Fluid Method for Sharp Interface Simulation of Plunging Breaking Waves," Int. J. Multi. Flow, 35(3), pp. 227-246.
[28] Shu, C.W. and Osher, S., 1988, "Efficient Implementation of Essentially non Oscillatory Shock-Capturing Schemes," J. Comput. Phys., 77(2), pp. 439-471.
[29] Jiang, G. and Peng, D., 1999, "Weighted ENO schemes for Hamilton-Jacobi equations," SIAM Journal. on Scientific Computing, 21(6), pp. 2126–2143.
[30] Leonard, B.P., 1979, "A Stable and Accurate Convective Modeling Procedure Based on Quadratic Upstream Interpolation," Computer Methods in Applied Mechanics and Engineering, 19, pp. 59–98.
[31] Balay, S., Gropp, W., McInnes, L., Smith, B., 1997, "Efficient Management of Parallelism in Object-Oriented Numerical Software Libraries," In Modern Software Tools in Scientific Computing, E. Arge, A. Bruaset, and H. Langtangen, Eds., Birkhauser Press, Cambridge, Mass., pp. 163-202
[32] Stern, F., Wilson, R. V., Coleman, H. W., and Paterson, E. G., 2001. "Comprehensive Approach to Verification and Validation of CFD Simulations-Part 1: Methodology and Procedures," ASME J. Fluids Eng., 123, pp. 793-802.
[33] Xing, T. and Stern, F., 2010, "Factors of Safety for Richardson Extrapolation," ASME J. Fluids Eng., in press.
[34] Huang, J., Carrica, P. M., and Stern, F., 2007, "Coupled Ghost Fluid/Two-Phase Level Set Method for Curvilinear Body-Fitted Grids," Int. J. Numer. Meth. Fluids, 55, pp. 867-897.
[35] Tian, Z., Perlin, M., and Choi, W., 2008, "Evaluation of a Deep-Water Wave Breaking Criterion," Phys. Fluids, 20(066604), pp. 1-13.
[36] Chang, K. A. & Liu, P. L. F., 1998, "Velocity, Acceleration and Vorticity under a Breaking Wave," Phys. Fluids, 10(1), pp. 327-329.
[37] Perlin, M., He, J., Bernal, L. P., 1996, "An Experimental Study of Deep Water Plunging Breakers," Phys. Fluids, 8(9), pp. 2365-2374.
[38] Shakeri, M., Tavakolinejad, M., and Duncan, J. H., 2009, "An Experimental Investigation of Divergent Bow Waves Simulated by a Two-Dimensional plus Temporal Wave Marker Technique," J. Fluid Mech., 634, pp. 217-243.
[39] Rapp, R. J. and Melville, W. K., 1990, "Laboratory Measurements of Deep-Water Breaking Waves," Phil. Trans. R. Soc. Lond. A, 331, pp. 735-800.
[40] Melville, W. K., Veron, F. and White, C. J., 2002. "The Velocity Field under Breaking Waves: Coherent Structures and Turbulence," J. Fluid Mech., 454, pp. 203-233.

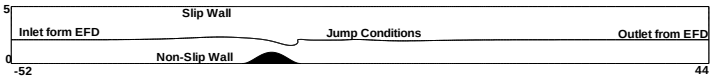

Figure 1 Computational domain.

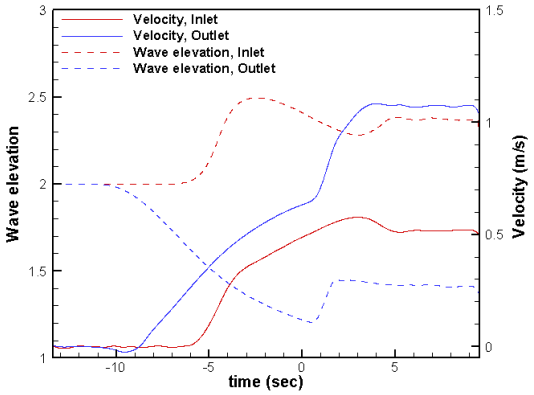

Figure 2 Experimental data used for CFD simulation.

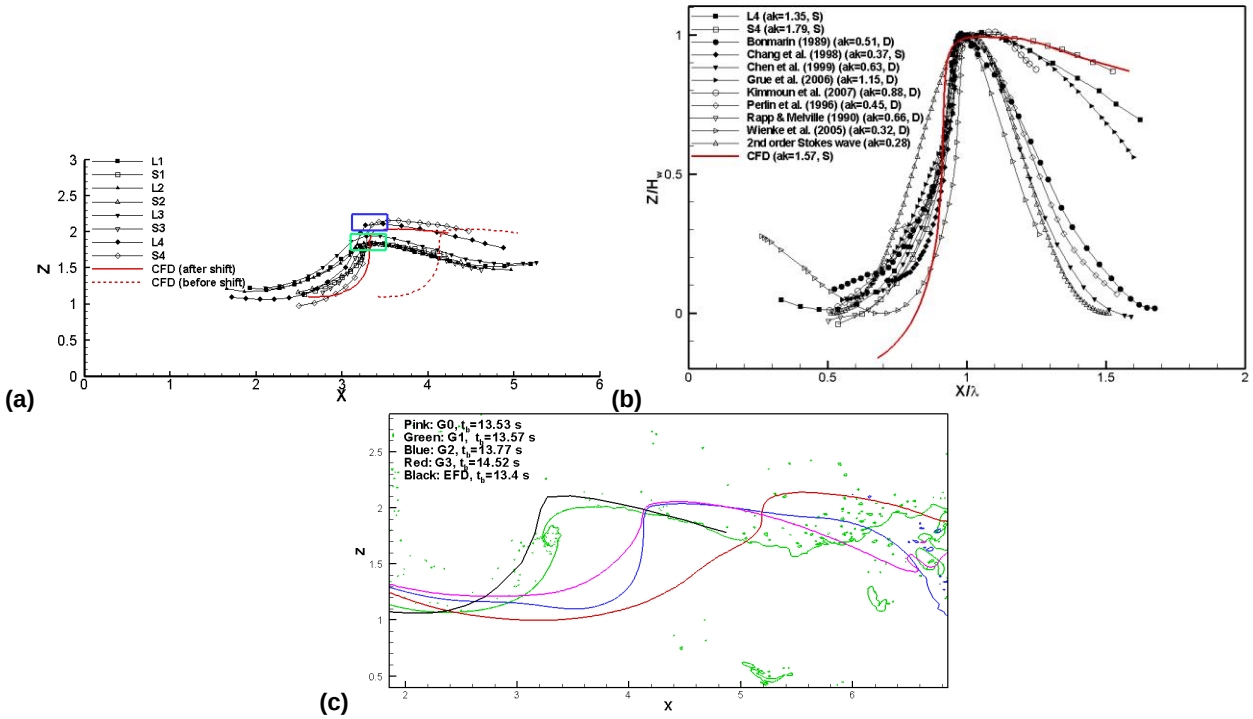

Figure 3 Wave profile comparison with experiments. (a) CFD profile shifted 0.81 in streamwise direction; (b) non-dimensional with wave length (λ) and wave height (H_w) at t_b in X, Z, respectively; (c) wave profiles at t_b.

Table 1 Plunging breaking wave with EFD

	EFD (L4)	G0	E (%)	Fine (G1)	E (%)	Medium (G2)	E (%)	Coarse (G3)	E (%)
t_b	13.4 s	13.53 s	1.0	13.57 s	1.26	13.77 s	2.7	14.52 s	8.3
x_b	3.38	4.33	28	3.39	0.3	4.26	26	5.24	55
z_b	2.14	2.04	4.7	1.97	7.9	2.03	5.1	2.09	2.3

Table 2 Verification study

Parameter	R_G	P_G	P	U_G%S_1
t_b	0.11	3.08	0.6	0.18
x_b	0.67	0.57	0.11	118
z_b	0.66	0.58	0.11	9.4

Table 3 Percentage of the plunging breaking wave time phase for each of the sub-events for experiments

Time	Δt_T = 14.8 s		%Δt_T					
-13.4 s	-		-				Startup	
-0.9 s	Δt_S = 12.5 s		84.5					
-	Δt_{SWF} = 0.9 s	-	6				Steep wave formation	
0.0 s		0.9 s						
-	Δt_{PWB} = 1.4 s	Δt		%Δt_{PWB}	Δt	9.5	Plunging wave breaking	1^{st} plunge
0.067 s		0.067 s	P1 38.1%	4.8	0.533			
0.133 s		0.066 s		4.7				1^{st} oblique splash
0.533 s		0.4 s		28.6				1^{st} vertical jet
0.6 s		0.067 s	P2 23.9%	4.8	0.334			2^{nd} plunge
0.667 s		0.067 s		4.8				2^{nd} oblique splash
0.867 s		0.2 s		14.3				2^{nd} vertical jet & 3^{rd} plunge
0.933 s		0.066 s	P3 19%	4.7	0.266			3^{rd} oblique splash
1.133 s		0.2 s		14.3				3^{rd} vertical jet & 4^{th} plunge
1.267 s		0.134 s	P4 19.1%	9.6	0.267			4^{th} oblique splash
1.4 s		0.133 s		9.5				4^{th} vertical jet

Table 4 Percentage of the plunging breaking wave time phase for each of the sub-events for CFD (G2)

Time	$\Delta t_T^{'}$ = 15.76 s		%$\Delta t_T^{'}$					
-13.77 s	-		-				Startup	
-0.95 s	Δt_S = 12.82 s		81.3					
-	Δt_{SWF} = 0.95 s	-	6				Steep wave formation	
0.0 s		0.95 s						
-	Δt_{PWB} = 1.99 s	Δt		%Δt_{PWB}	Δt	12.6	Plunging wave breaking	
0.16 s		0.16 s	P1 19.1%	8	0.38			1st plunge
0.19 s		0.03 s		1.5				1st oblique splash
0.38 s		0.19 s		9.5				1st vertical jet
0.91 s		0.53 s	P2 33.2%	26.6	0.66			2nd plunge
0.98 s		0.07 s		3.5				2nd oblique splash
1.04 s		0.06 s		3				2nd vertical jet
1.55 s		0.51 s	P3 27.1%	25.7	0.54			3rd plunge
1.58 s		0.03 s		1.5				3rd oblique splash
1.83 s		0.25 s	P4 20.6%	12.7	0.41			4th plunge
1.89 s		0.06 s		3				4th oblique splash
1.99 s		0.1 s		5				4th vertical jet

Table 5 Time interval of each plunging phase

Plunging phase	EFD (L4)	G0	G2	G3
P1	0.533 s	0.4 s	0.38 s	0.54 s
P2	0.334 s	1.35 s	0.66 s	0.31 s
P3	0.266 s	0.19 s	0.54 s	0.31 s
P4	0.267 s	0.43 s	0.41 s	0.33 s

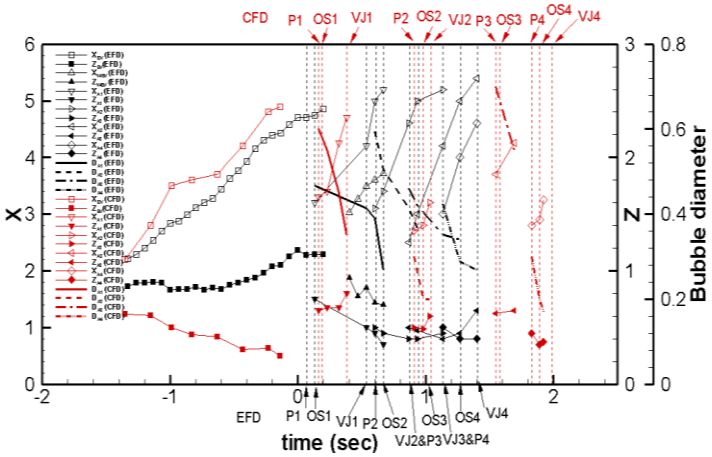

Figure 4 Time history of vortex and air entrainment paths, and air bubble size. Red: CFD; black: experiments.

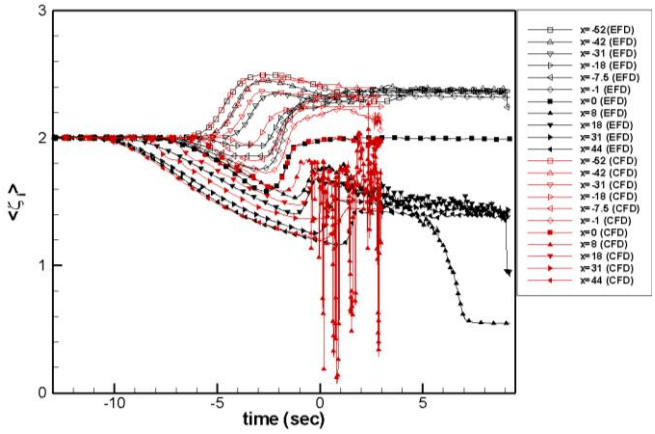

Figure 5 Time history of water elevations.

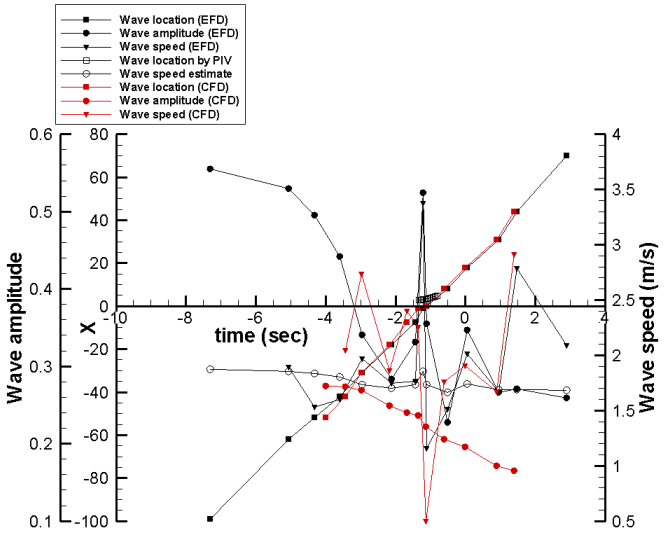

Figure 6 Time history of acceleration wave location, speed, and amplitude

Figure 7 is shown on next page.

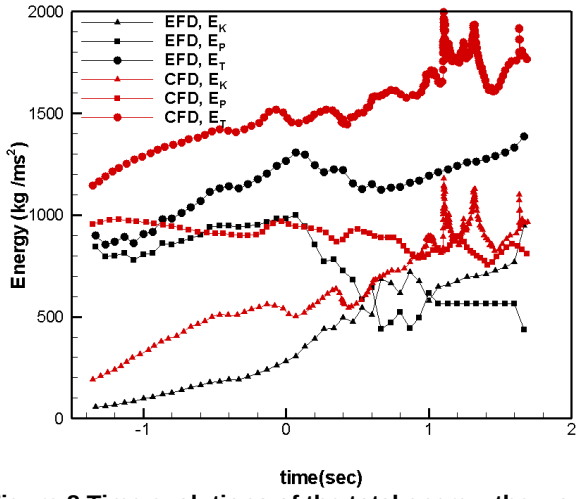

Figure 8 Time evolutions of the total energy, the wave kinetic energy, the wave potential energy.

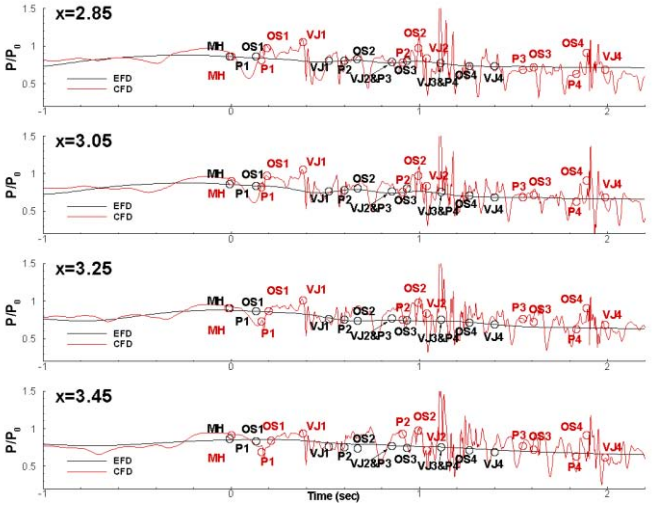

Figure 9 Average pressure time series for experiments and CFD at various stream-wise positions.

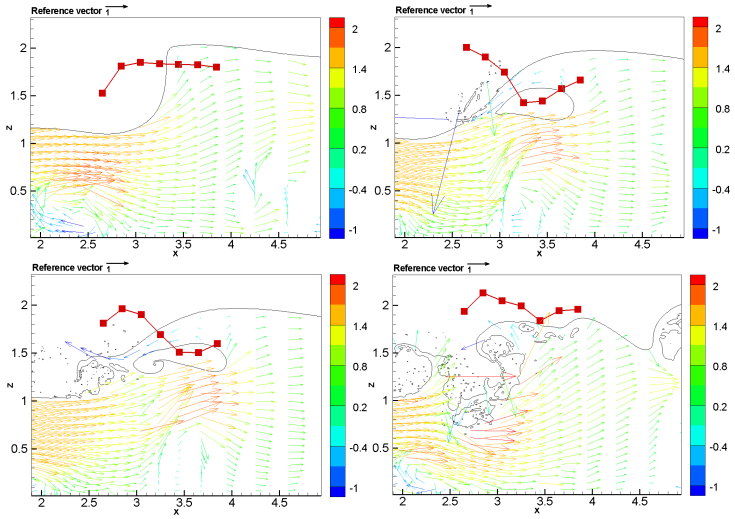

Figure 10 CFD velocity vector field, wave elevations and bottom pressure distribution.

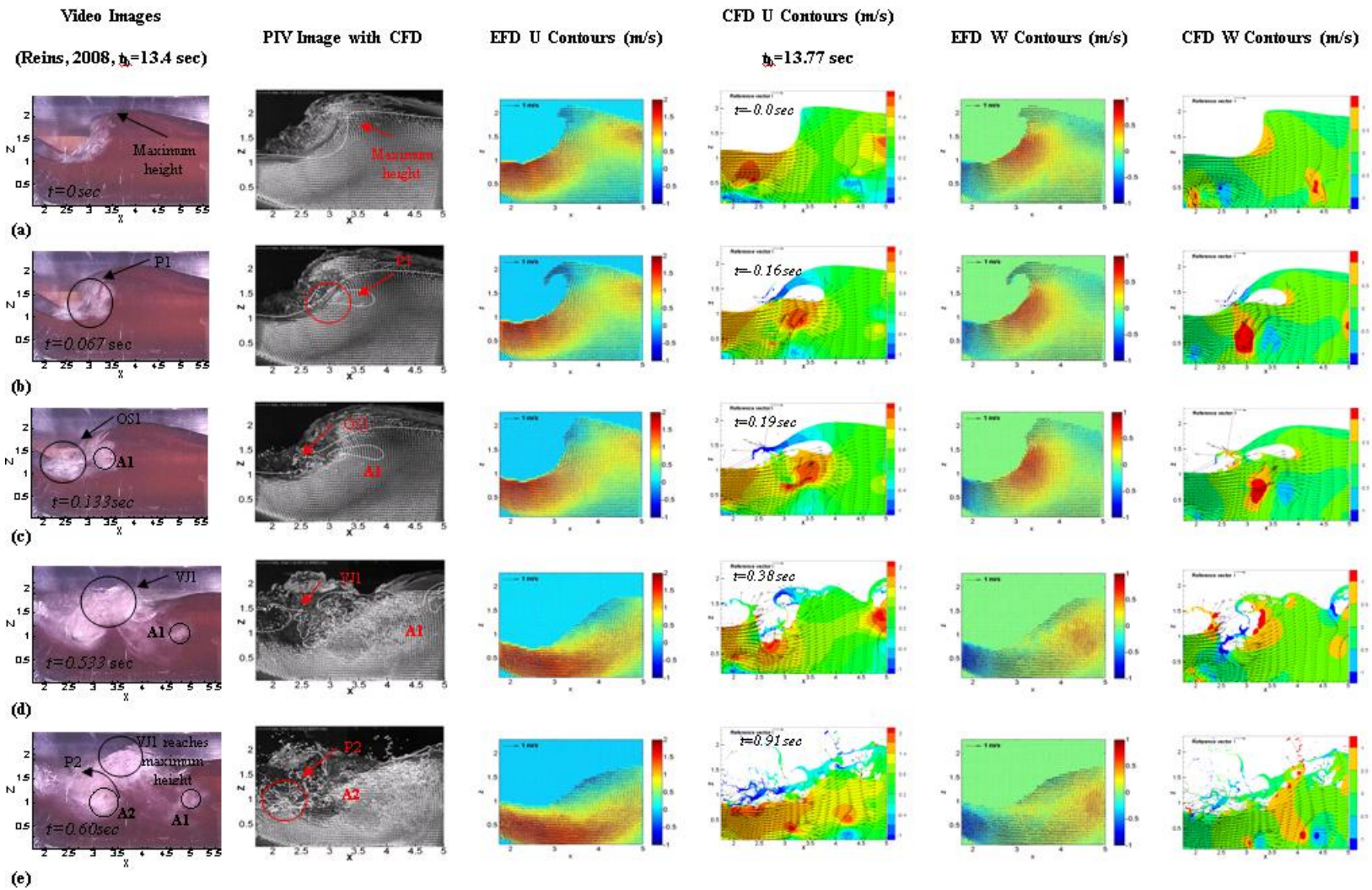

Figure 7 Video images; PIV image with CFD; experimental U velocity contours; CFD U velocity contours; experimental W velocity contours; CFD W velocity contours.